RSC Advances

PAPER

View Article Online
View Journal | View Issue

Check for updates

Cite this: *RSC Adv.*, 2020, **10**, 30214

Ultrasonic-assisted preparation of highly active Co_3O_4/MCM-41 adsorbent and its desulfurization performance for low H_2S concentration gas

Bolong Jiang, *[a] Jiaojing Zhang, [b] Yanguang Chen,[b] Hua Song, *[b] Tianzhen Hao[c] and Junhu Kuang[d]

Co_3O_4/MCM-41 adsorbents were successfully prepared by ultrasonic assisted impregnation (UAI) and traditional mechanical stirring impregnation (TMI) technologies and characterized by X-ray diffraction (XRD), N_2 adsorption desorption, Fourier transform infrared spectra (FT-IR), transmission electron microscopy (TEM), scanning electron microscopy (SEM) and thermogravimetry-differential thermal analysis (TG-DTA). The H_2S removal performances for a simulated low H_2S concentration gas were investigated in a fixed-bed. The effect of preparation and adsorption conditions on the H_2S removal over Co_3O_4/MCM-41 were systematically examined. The results showed that UAI promotes more and well defined highly dispersed active Co_3O_4 phase on MCM-41. As compared to the Co_3O_4/MCM-41-T prepared *via* TMI, the saturated H_2S capacity of Co_3O_4/MCM-41-U prepared *via* UAI improved by 33.2%. The desulfurization performance of adsorbents decreased in the order of Co_3O_4/MCM-41-U > Co_3O_4/MCM-41-T > MCM-41. The Co_3O_4/MCM-41-U prepared using $Co(NO_3)_2$ concentration of 10%, ultrasonic time of 2 h, calcination temperature of 550 °C and calcination time of 3 h exhibited the best H_2S removal efficiency. At adsorption temperature of 25 °C with model gas flowrate of 20 mL min^{-1}, the breakthrough time of Co_3O_4/MCM-41-U was 10 min, and the saturated H_2S capacity and H_2S removal rate was 52.6 mg g^{-1} and 47.8%, respectively.

Received 27th June 2020
Accepted 6th August 2020

DOI: 10.1039/d0ra05606e

rsc.li/rsc-advances

Open Access Article. Published on 17 August 2020. Downloaded on 2/10/2026 6:04:56 PM.
This article is licensed under a Creative Commons Attribution-NonCommercial 3.0 Unported Licence.

1 Introduction

Industrial processes have produced large amount of hazardous materials which are harmful for humans and the environment.[1,2] Hydrogen sulfide (H_2S) with its characteristic rotten egg smell is often present in a variety of hydrocarbon resources such as natural gas and biogas.[3] H_2S is a poisonous, corrosive and flammable colorless gas. Therefore, removing this poisonous gas from hydrocarbon resources is an important global concern.[4]

Currently, methods of H_2S removal from hydrocarbon resources are mainly wet and dry desulfurization. An alcohol amine solution is commonly used in industrial H_2S absorption.[5,6] However, disadvantages of this method for industrial application are large investment and high energy consumption. Comparatively, the dry method is preferred over the wet method in terms of cost and environmental considerations. Moreover, adsorption is known as one of the most efficient candidates to adsorb H_2S from low H_2S concentration gases owing to its ability to produce a very low H_2S level gas under moderate conditions.[7] So far, several types of adsorbents such as zeolites, activated carbons, metal organic frameworks, clays and molecular sieves have been investigated in dry adsorption of H_2S.[8,9] However, low sulfur capacity and selectivity of these unmodified adsorbents requires frequent regeneration of spent adsorbents.[10] In this concern, developing an adsorbent with a high sulfur capacity to achieve the targeted removal and a long lifetime are of great important.[11] Metal oxides, such as iron, zinc, manganese, copper and calcium oxides, have been widely investigated for H_2S removal.[12–14] Metal oxides adsorb H_2S *via* a chemical reaction, which produces a metal sulfide. However, using metal oxides directly in their pure forms has several drawbacks. The main drawbacks are the difficult recovering and reusability properties, low adsorption properties owing to the low surface area and poor mass transfer ability of metal oxides, which limits their application for H_2S removal. An effective way to address the above drawbacks is to support metal oxides on high surface supports.[15] Therefore, transition metal oxides loaded on proper supports have been widely investigated.[16] The MCM-41 is commonly used as support in catalyst field, due to its high surface area, tunable pore diameter and large pore

[a]*Innovation Institute for Sustainable Maritime Architecture Research and Technology, Qingdao University of Technology, Qingdao 266000, China. E-mail: jiangbolong@qut.edu.cn; Fax: +86 532 85071522; Tel: +86 532 85071522*
[b]*Provincial Key Laboratory of Oil & Gas Chemical Technology, College of Chemistry & Chemical Engineering, Northeast Petroleum University, Daqing 163318, Heilongjiang, China. E-mail: songhua2004@sina.com; Fax: +86 459 6503167; Tel: +86 459 6503167*
[c]*Hebei Jingzhi Technology Company Ltd., Cangzhou 061000, Hebei, China*
[d]*Yumen Oilfield Company Refining and Chemical Plant, 735200, Gansu, China*

This journal is © The Royal Society of Chemistry 2020

Open Access Article. Published on 17 August 2020. Downloaded on 2/10/2026 6:04:56 PM.
This article is licensed under a Creative Commons Attribution-NonCommercial 3.0 Unported Licence.

volume.[17,18] However, unmodified MCM-41 is poor in desulfurization due to the main adsorption way of which is physical adsorption. In this regard, supporting active metal oxide on MCM-41 porous materials is expected to be an effective way to take full advantages of metal oxides and MCM-41.[10,19]

It is well known that loading method would greatly affect the dispersion of metal oxide on surface of support, which in turn affect its H_2S removal performance.[20] Ultrasonic assisted impregnation (UAI) has recently received much attention as its unique dispersion properties. The dispersion of active metal oxides on surface of support can be greatly improved by using this technique because ultrasonic wave can produce a powerful microjet flow through its "cavitation effect", which in turn produce a great impact on the support.[21] In addition, the harsh operating conditions (such as high temperatures), which usually needed to achieve a better dispersion for traditional mechanical stirring impregnation (TMI) methods, are not required. Mi *et al.*[22] reported that as compared to TMI method, metal oxides can more evenly be dispersed in char when the UAI technology was applied.

Cobalt oxide, as well as its based composites, was investigated extensively as potential materials in many fields.[23] Silas *et al.*[24] synthesized activated carbon monolith supported tricobalt tetraoxide (Co_3O_4) adsorbent (Co_3O_4/ACM) for simultaneous SO_2/NO_x removal from flue gas and found that the Co_3O_4/ACM adsorbent exhibited a high affinity to NO_x adsorption. Therefore, it is reasonable to expect that combining the advantage of Co_3O_4 and high surface mesoporous MCM-41, coupled with UAI technology, might yield unexpected adsorbent for efficient H_2S removal. However, to the best of our knowledge, adsorbents based on Co_3O_4 supported on MCM-41 prepared by UAI for the H_2S removal from natural gas have not been reported. Therefore, we believe that Co_3O_4/MCM-41 adsorbent prepared by UAI method is worth studying.

In the present work, Co_3O_4/MCM-41 was prepared by UAI and TMI technologies, and their adsorptive removal performances for a simulated low H_2S concentration gas were investigated. As expected, Co_3O_4/MCM-41 prepared by UAI technology exhibited much higher surface area and H_2S removal performance. In addition, the effect of preparation and adsorption conditions on the H_2S removal performance of Co_3O_4/MCM-41 were systematically examined.

2 Experimental

2.1 Adsorbents preparation

The cobalt oxide supported mesoporous MCM-41 was prepared by ultrasonic assisted impregnation (UAI) method (Scheme 1). First, 1 g of precalcined MCM-41 (all-silicon, Nankai University Catalyst Factory) was dispersed in 25 mL cobalt nitrate ($Co(NO_3)_2 \cdot 6H_2O$) solution with cobalt nitrate concentration of 10% and treated by ultrasonic wave for 2 h. The suspension was then filtered and washed with ethanol (Haerbin Chemical Reagent Company) and distilled water in turn, followed by drying in the oven at 110 °C for 12 h. Then the solid was transferred to muffle furnace and calcined at 550 °C for 3 h. The

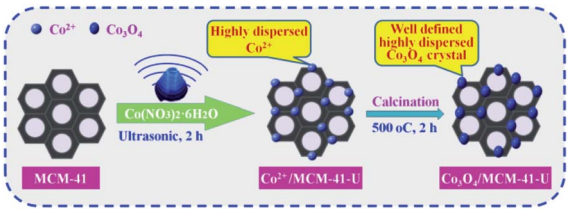

Scheme 1 Schematic diagram for the synthesis of Co_3O_4/MCM-41-U *via* ultrasonic assisted impregnation.

obtained sample named as Co_3O_4/MCM-41-U, where U means prepared by UAI method. For comparison, the Co_3O_4/MCM-41 was also prepared by traditional impregnation (mechanical stirring for 24 h) method (TMI) with other conditions remained unchanged, which denoted as Co_3O_4/MCM-41-T. The Co_3O_4/MCM-41-U samples were also prepared at different conditions by varying the cobalt nitrate concentration (5%, 8%, 10%, 13% and 15%), ultrasound time (1.5 h, 2 h, 2.5 h and 3 h), calcination temperature (350 °C, 450 °C, 550 °C and 650 °C)and time (2 h, 3 h, 4 h and 5 h).

2.2 Characterization

The X-ray diffraction (XRD) measurement and analysis were obtained from X-ray diffractometer (a D/max-2200PC-X-ray diffractometer) by using Cu Kα radiation conducted at 40 kV, 30 mA, and a scan range from 10° to 80° at a rate of 10° min^{-1}. The typical physicochemical properties of the supports and catalysts were analyzed were analyzed by N_2-adsorption specific surface area measurements using the Brunauer–Emmett–Teller (BET, Micromeritics, NOVA 2000e: Surface Area & Pore Size Analyzer). The Fourier transform infrared spectra (FT-IR) of the catalysts were recorded with a Brook Tensor 27 Fu Liye infrared spectrometer in the optical range of 400–4000 cm^{-1}. The thermal stability of adsorbent was analyzed by (TG-DTA DuPont 2100) with heating rate: 10 K min^{-1} under the protect flow of 20 mL min^{-1}. The reducibility of precursors was characterized by the H_2 temperature-programmed reduction (H_2-TPR) using (CHEMBET-3000, Quantachrome) a quartz U-tube reactor (inner diameter of 6 mm). Reduction was conducted at a heating rate of 10 K min^{-1} in a 5 vol% H_2/N_2 flow (30 mL min^{-1}).

2.3 Fixed-bed ADS experiment

Measurements of adsorbent activity were conducted in a fixed-bed reactor (Scheme 2). The fixed-bed reactor (a quartz glass

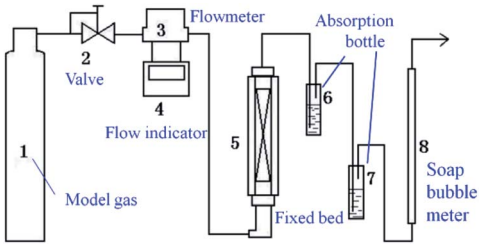

Scheme 2 Schematic diagram of the experimental apparatus.

Open Access Article. Published on 17 August 2020. Downloaded on 2/10/2026 6:04:56 PM.
This article is licensed under a Creative Commons Attribution-NonCommercial 3.0 Unported Licence.

tube with diameter of 10 mm and length of 300 mm) placed vertically in a furnace. Typically, 0.2 g adsorbent was loaded into the reactor. The model fuel gas (H_2S, N_2 and O_2 mixture; N_2 as balance gas; the H_2S concentration was 20 mg L^{-1}) from a feed tank passed through a reducing valve and entered into the reactor at a flowrate of 20 mL min^{-1}. Any unadsorbed H_2S gas in the effluent gas would be absorbed by the liquid in the absorption bottle, and the H_2S content of the absorption liquid was determined by iodometry at intervals of 5 min. The saturated H_2S capacity and H_2S removal rate of the absorbent were calculated by the analysis of H_2S breakthrough curves.

The saturated H_2S capacity is defined as the amount of adsorbed H_2S per gram of adsorbent when the H_2S concentrations in the effluent and in the initial gas are the same. It can be calculated as follows.[10]

$$q_m = \frac{V \times \omega_{H_2S} - \left(c_{I_2} v_{I_2} - 0.5 c_{Na_2S_2O_3} v_{Na_2S_2O_3}\right) \times 34}{m} \quad (1)$$

where q_m is the saturated H_2S capacity, mg g^{-1}; ω is the H_2S concentration in the model gas, mg L^{-1}; V is the total gas volume, L; c is the concentration in mol L^{-1}; v is the volume in L; m is amount of adsorbent, g; and 34 is the molar mass of H_2S in g mol^{-1}.

The H_2S removal rate η can be expressed as

$$\eta = \frac{V \times \omega_{H_2S} - \left(c_{I_2} v_{I_2} - 0.5 c_{Na_2S_2O_3} v_{Na_2S_2O_3}\right) \times 34}{V \times \omega_{H_2S}} \times 100\% \quad (2)$$

2.4 Calculation of mass transfer zone

The mass transfer zone (MTZ) can be defined as the following equation:[25]

$$MTZ = \frac{(\tau_e - \tau_a)}{\tau_e} \times Z_o \quad (3)$$

where MTZ is the mass transfer zone with the unit of mm; τ_a is the breakthrough time to reach $c/c_0 = 0.10$; τ_e is the saturated adsorption time to reach $c/c_0 = 0.95$; Z_o stands for the height of fixed bed column with the unit of mm (300 mm in this study).

3 Results and discussion

3.1 Characterization of adsorbents

3.1.1 XRD. As can be seen in Fig. 1, all the samples showed a strong broad peak at 2θ = 15–30° due to the amorphous nature of mesoporous MCM-41, showing the mesopores of MCM-41 were retained after successive impregnation and high temperature calcination.[26,27] The Co_3O_4/MCM-41-T which prepared by traditional impregnation (TMI) method showed diffraction peaks at 2θ = 36.8°, 44.8°, 59.3° and 65.2°, which corresponded the cubic phase Co_3O_4 lattice planes of (311), (400), (511) and (440) [PDF # 23-1003][28], respectively. For the Co_3O_4/MCM-41-U which obtained *via* ultrasonic assisted impregnation (UAI) method, the diffraction peaks at 2θ = 19°, 31.27°, 36.8°, 38.5°, 44.8°, 55.6°, 59.3° and 65.2° were observed, which can be assigned to the cubic phase Co_3O_4 lattice planes of (111), (220), (311), (222), (400), (422), (511) and (440), respectively.[29] This demonstrated that the cobalt oxide obtained by calcination the precursor was Co_3O_4 phase. It is interesting to note that all the diffraction peaks of the as-synthesized Co_3O_4 can be seen for Co_3O_4/MCM-41-U, but some peaks were disappeared for Co_3O_4/MCM-41-U, showing the UAI produce more and well defined regularly sorted Co_3O_4 crystal phase.

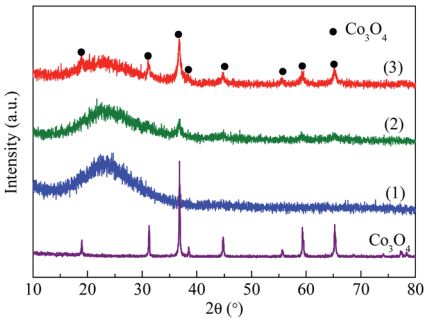

Fig. 1 XRD patterns of blank MCM-41 and adsorbents prepared by different methods. (1) MCM-41, (2) Co_3O_4/MCM-41-T and (3) Co_3O_4/MCM-41-U.

3.1.2 BET. The nitrogen adsorption isotherms, pore size distributions and textural properties of MCM-41, Co_3O_4/MCM-41-T and Co_3O_4/MCM-41-U are shown in Fig. 2 and Table 1. According to the new IUPAC technical report,[30] the isotherms of the these three samples identified as type IV isotherms, which is characteristic of microporous materials. And the hysteresis loop is classified as H1 type, which corresponds to the tubular pore model with openings at both ends.[31] However, the inflection pressure and the slope of these curves at each stage are somewhat different after loading of Co_3O_4. From the position of the hysteresis loop appeared, the average diameter of the pores can be estimated approximately 3 nm, which was consistent with

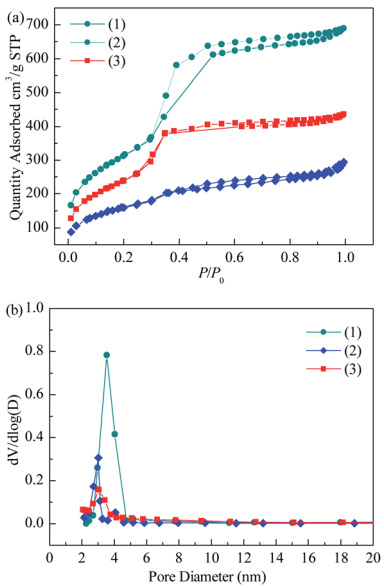

Fig. 2 N_2 adsorption–desorption isotherm (a) and BJH pore size distribution (b) of blank MCM-41 and adsorbents prepared by different methods.

This journal is © The Royal Society of Chemistry 2020

Open Access Article. Published on 17 August 2020. Downloaded on 2/10/2026 6:04:56 PM.
This article is licensed under a Creative Commons Attribution-NonCommercial 3.0 Unported Licence.

Table 1 The pore structures of blank MCM-41 and adsorbents prepared by different methods

Sample	Surface area ($m^2\ g^{-1}$)	Pore volume ($cm^3\ g^{-1}$)	Pore diameter (nm)
MCM-41	1140.7	1.07	3.74
Co_3O_4/MCM-41-T	648.6	0.45	2.75
Co_3O_4/MCM-41-U	919.2	0.67	2.93

the average pore diameter of 3.74, 2.75 and 2.93 nm (see Table 1), respectively. The low pressure hysteresis loop can be considered to be caused by capillary condensation of N_2 in the straight channel of MCM-41 itself.[32] The high pressure hysteresis loop may be caused by capillary condensation of N_2 between interparticles of MCM-41.[33] For Co_3O_4/MCM-41-T and Co_3O_4/MCM-41-U, the hysteresis loop within the p/p_0 range of 0.45–0.65 indicates the ordered structure and uniform mesoporous channel of the MCM-41 were retained after loading of Co_3O_4. These results are consistent with the XRD results. As can be seen from Fig. 2 that the pores of blank MCM-41 were ranged in 2–5 nm. Upon loading of Co_3O_4 on MCM-41, the pore size decreased, showing the Co_3O_4 entered into the pores. The specific surface area and pore volume of blank MCM-41 were up to 1095.2 $m^2\ g^{-1}$ and 1.22 $cm^3\ g^{-1}$ (Table 1). The loading of Co_3O_4 caused the decrease in specific surface area and pore volume. However, the decrease was less severe for Co_3O_4/MCM-41-U than that of Co_3O_4/MCM-41-T, which possibly because the UAI promotes evenly dispersed small Co_3O_4 particles on surface of the MCM-41.[21]

3.1.3 FT-IR. The surface functional groups on the samples were examined by Fourier-transform infrared (FTIR) spectra (Fig. 3). The similarity of the FTIR spectra of these three samples, featured the absorption peaks at the same wavelengths, showed that the types of functional groups of MCM-41 were basically remained after modification.[34] For MCM-41, the peak appeared at 1634 cm^{-1} can be attributed to physically adsorbed water. However, the intensity of this peak was reduced for Co_3O_4/MCM-41-T and Co_3O_4/MCM-41-U, showing the loss of water.[35] The characteristic peaks at 450, 807, 1085 and 1250 cm^{-1} is classified as the vibration of Si–O–Si.[36] For Co_3O_4/MCM-41-T and Co_3O_4/MCM-41-U, a new absorption peaks

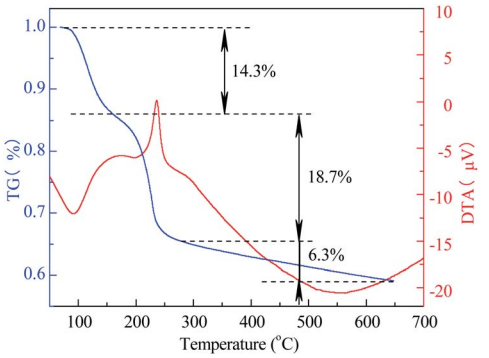

Fig. 4 TG-DTA curves of Co_3O_4/MCM-41 precursor without calcination.

appeared at 960 cm^{-1} as compared to the blank MCM-41. For the appearance of this shoulder peak, two different points of view have been proposed. Some researchers suggested that it is owing to the introduction of the heteroatom in the skeleton, while others suggested that it is owing to the asymmetry of the partial skeleton structure arising from defect sites.[37] Moreover, the new absorption peaks appeared at 660 cm^{-1} and 562 cm^{-1} belong to the stretching vibration of spinel phase Co–O in Co_3O_4,[38,39] which confirms the formation of Co_3O_4. It should be noted that the intensities of these two peaks of Co_3O_4/MCM-41-U were obviously stronger than those of Co_3O_4/MCM-41-T, showing UAI promotes formation of more Co_3O_4 crystal active phase.

3.1.4 TG-DTA. The TG-DTA curve of Co_3O_4/MCM-41-U is shown in Fig. 4. For temperature range of 0–150 °C, the TG curve showed a weight loss of 14.3%, which corresponds to a strong endothermic peak in DTA curve. This weight loss can be assigned to the elimination of adsorbed water from the surface and pores.[40] While for the temperature range of 150–260 °C, the TG curve exhibited a weight loss of 18.7%, which corresponds to a sharp exothermal peak in DTA curve. This weight loss can be assigned to the decomposition of $Co(NO_3)_2$ in precursor to Co_3O_4. For the temperature higher than 260 °C to 650 °C, the weigh loss became extremely slow (6.3%). This weight loss can be assigned to the sintering or decomposition of components and dehydration of adsorbent at high temperature.[41]

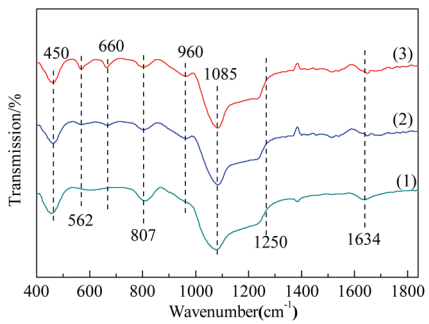

Fig. 3 The H_2-TPR profiles of blank MCM-41 and adsorbents prepared by different methods. (1) MCM-41, (2) Co_3O_4/MCM-41-T and (3) Co_3O_4/MCM-41-U.

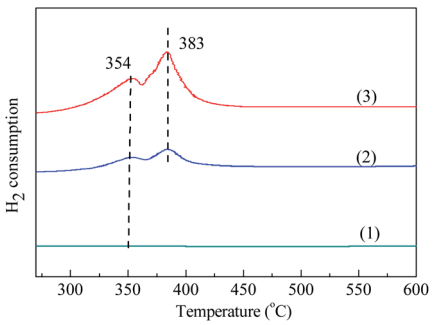

Fig. 5 The H_2-TPR profiles of blank MCM-41 and adsorbents prepared by different methods. (1) MCM-41, (2) Co_3O_4/MCM-41-T and (3) Co_3O_4/MCM-41-U.

Open Access Article. Published on 17 August 2020. Downloaded on 2/10/2026 6:04:56 PM.
This article is licensed under a Creative Commons Attribution-NonCommercial 3.0 Unported Licence.

3.1.5 TPR. Fig. 5 shows the H_2-TPR curves of these three samples. It can be observed that two reduction peaks presented at temperature range of 100–600 °C. The reduction peak at lower temperature of 354 °C can be ascribed to the H_2 consumption due to the reduction of Co_3O_4 to CoO, while the reduction peak at higher temperature of 383 °C can be ascribed to the H_2 consumption owing to the reduction of CoO to Co.[42] The corresponding reduction reactions are shown as follows:

$$Co_3O_4 + H_2 = 3CoO + H_2O \quad (4)$$

$$CoO + H_2 = Co + H_2O \quad (5)$$

It should be noted that the intensity of these two peaks of Co_3O_4/MCM-41-U was obviously stronger than those of Co_3O_4/MCM-41-T, showing UAI promotes formation of more Co_3O_4 crystal active phase. This observations are consistent with the results obtained in the FT-IR.

3.2 Adsorptive desulfurization

3.2.1 Effect of preparation methods. The adsorbents were evaluated at 25 °C with model gas flowrate of 20 mL min^{-1} in the fixed-bed reactor using 0.2 g of adsorbent (Fig. 6). It can be seen that the breakthrough time of blank MCM-41 is the shortest. Upon loading of Co_3O_4 on MCM-41, the breakthrough time extended, showing loading of Co_3O_4 can enhance the H_2S removal efficiency. The saturated H_2S capacity of adsorbent showed similar tends. The saturated H_2S capacity of Co_3O_4/MCM-41-T and Co_3O_4/MCM-41-U were 18.4 and 24.5 mg g^{-1}, respectively, which are increased by 23.5% and 64.4% as compared to that of the original MCM-41. It should be noted that the Co_3O_4/MCM-41-U prepared *via* UAI showed a better H_2S removal performance than that of Co_3O_4/MCM-41-T prepared *via* TMI. This is possibly because UAI promotes more and well defined highly dispersed active Co_3O_4 phase (see XRD, FT-IR and TPR analysis) loading on the MCM-41 due to its "cavitation effect", and therefore would lead to a higher H_2S removal efficiency (Scheme 3). Moreover, Co_3O_4/MCM-41-U possessed a higher surface area (BET analysis) as compared to that of Co_3O_4/MCM-41-T, which facilitate exposure more active sites to H_2S. The similar results were observed by Dou,[21] who found that Fe–Zn supported on activated-char *via* UAI showed much better performance than that *via* TMI. They explained that UAI enhanced the chemical reaction and mass transfer *via* acoustic cavitation during preparation process,[43] which can improve the H_2S removal performance. The H_2S removal performance of the adsorbents decreased in the order of Co_3O_4/MCM-41-U > Co_3O_4/MCM-41-T > MCM-41.

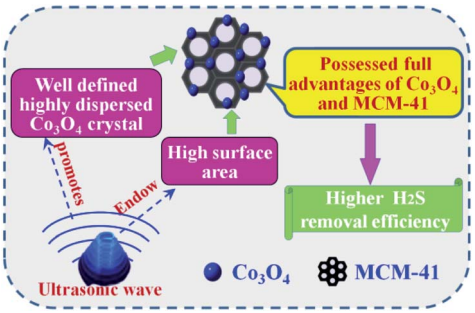

Scheme 3 Explanation for the improved H_2S removal efficiency over Co_3O_4/MCM-41-U.

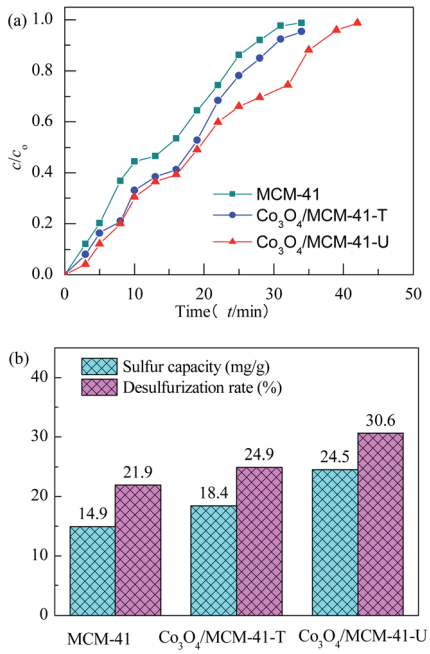

Fig. 6 H_2S breakthrough curves (a) and saturated H_2S capacity and desulfurization rate (b) of samples prepared by different methods.

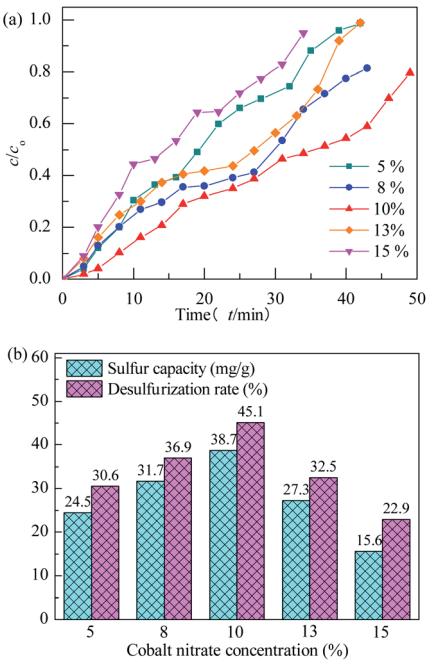

Fig. 7 H_2S breakthrough curves (a) and saturation sulfur capacity and desulfurization rate (b) of Co_3O_4/MCM-41-U prepared using different cobalt nitrate concentration.

This journal is © The Royal Society of Chemistry 2020

Open Access Article. Published on 17 August 2020. Downloaded on 2/10/2026 6:04:56 PM.
This article is licensed under a Creative Commons Attribution-NonCommercial 3.0 Unported Licence.

3.2.2 Effect of preparation conditions. All of the adsorbents were evaluated at adsorption temperature of 25 °C with model gas flowrate of 20 mL min^{-1} in the fixed-bed reactor using 0.2 g of adsorbent in this section. The effect of concentration of $Co(NO_3)_2$ on performance of H_2S removal over Co_3O_4/MCM-41-U is shown in Fig. 7. With increasing the concentration of $Co(NO_3)_2$, the breakthrough and saturated adsorption time both increased first and then decreased, reached the maximums at $Co(NO_3)_2$ concentration of 10%, which are 7 min and 53 min, respectively. This is possibly because that for the very low $Co(NO_3)_2$ concentration, the loading of active Co_3O_4 on adsorbent would be low, which in turn led to a poor H_2S adsorption. However, with an excess of active Co_3O_4 loading, the agglomeration of Co_3O_4 and blockage of some pores of adsorbent would occur, which could decrease the H_2S removal performance. The saturated H_2S capacity and desulfurization rate of adsorbents exhibited the similar trends, which shows the maximum saturated H_2S capacity and desulfurization rate of 38.7 and 45.1%, respectively, at $Co(NO_3)_2$ concentration of 10%.

The effect of ultrasonic time on performance of H_2S removal over Co_3O_4/MCM-41-U with $Co(NO_3)_2$ concentration of 10% remained unchanged is shown in Fig. 8. With increasing the ultrasonic time, the breakthrough and saturated adsorption time both increased first and then decreased, reached the maximums at ultrasonic time of 2 h, which are 7 min and 53 min, respectively. Ultrasonic wave, can produce a powerful microjet flow *via* its "cavitation effect", which in turn can produce a great impact on the support. As a results, the active components can be more evenly dispersed in the support channel, and thus UAI improves the H_2S removal activity. However, when ultrasonic time is too long, it would causes a local accumulation of Co species at the standing wave node of ultrasonic and lead to a poor dispersion of active Co_3O_4 on support, which in turn decreases the H_2S removal performance. The saturated H_2S capacity and desulfurization rate of adsorbents exhibited the similar trends, which shows the maximum saturated H_2S capacity and desulfurization rate of 38.7 and 45.1%, respectively, at ultrasonic time of 2 h.

The effect of calcination temperature on performance of H_2S removal over Co_3O_4/MCM-41-U with $Co(NO_3)_2$ concentration of 10% and ultrasonic time of 2 h remained unchanged is shown in Fig. 9. With increasing the calcination temperature, the breakthrough and saturated adsorption time both increased first and then decreased, reached the maximums at calcination temperature of 550 °C, which are 7 min and 53 min, respectively. The calcination is a thermal treatment process which will bring about a thermal decomposition, phase transition, or removal of a volatile fraction. The TG-DTA analysis is evident that the decomposition of $Co(NO_3)_2$ occurred between 150–260 °C and continued weight loss till 650 °C owing to the sintering or decomposition of components at high temperature. From XRD analysis, it can be known that at 550 °C, the metal oxide was well defined Co_3O_4 crystal phase, which is high in activity. Further increase the calcination temperature would cause the sintering, which would lead to an aggregation of active Co_3O_4 and thus poor H_2S removal efficiency.[44] The saturated H_2S capacities of the adsorbents decreased in the order: 550 °C > 450 °C > 650 °C > 350 °C. The calculated values were 38.7, 26.2, 26.1 and 23.5 mg g^{-1}, respectively. The saturated H_2S capacity and desulfurization rate of adsorbents exhibited the similar trends, which shows the maximum saturated H_2S

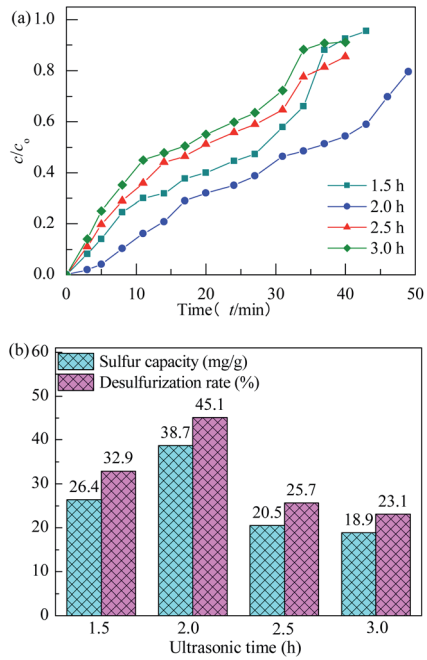

Fig. 8 H_2S breakthrough curves (a) and saturation sulfur capacity and desulfurization rate (b) of Co_3O_4/MCM-41-U prepared at different ultrasonic times.

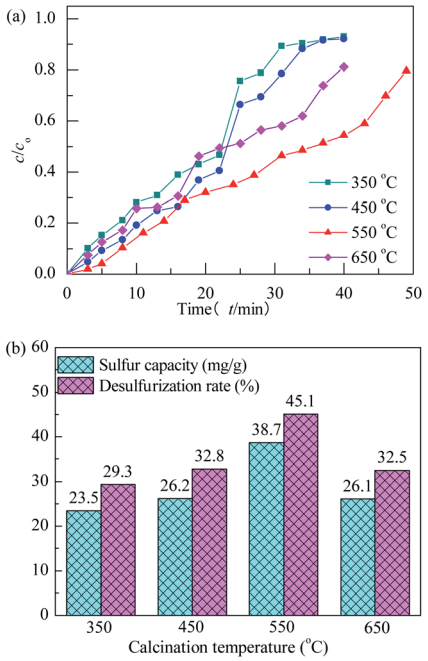

Fig. 9 H_2S breakthrough curves (a) and saturation sulfur capacity and desulfurization rate (b) of Co_3O_4/MCM-41-U prepared at different calcination temperatures.

Open Access Article. Published on 17 August 2020. Downloaded on 2/10/2026 6:04:56 PM.
This article is licensed under a Creative Commons Attribution-NonCommercial 3.0 Unported Licence.

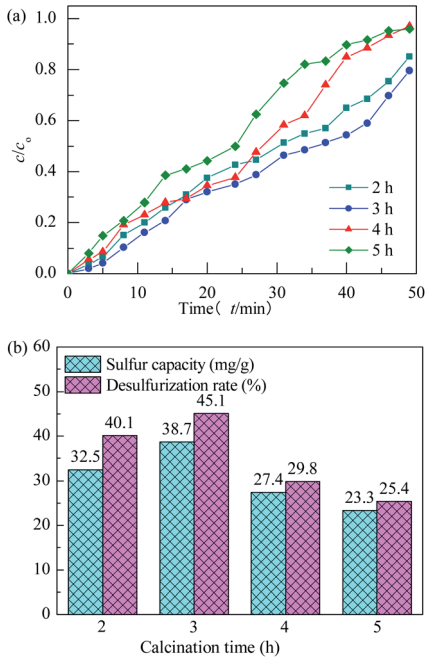

Fig. 10 H_2S breakthrough curves (a) and saturation sulfur capacity and desulfurization rate (b) of Co_3O_4/MCM-41-U prepared at different calcination times.

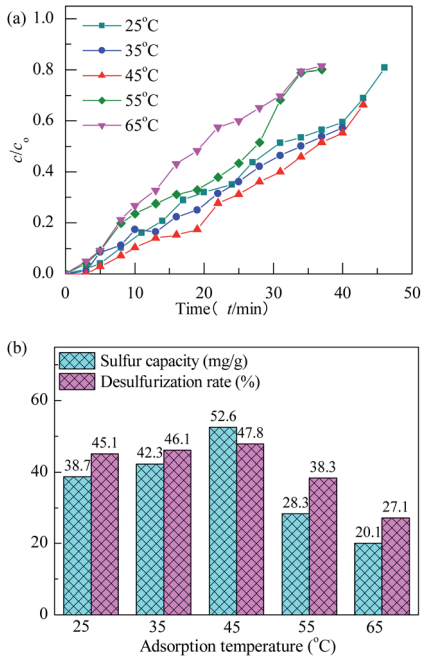

Fig. 11 H_2S breakthrough curves (a) and saturation sulfur capacity and desulfurization rate (b) of Co_3O_4/MCM-41-U at different adsorption temperatures.

capacity and desulfurization rate of 38.7 and 45.1%, respectively, at calcination temperature of 550 °C.

The effect of calcination time on performance of H_2S removal over Co_3O_4/MCM-41-U with $Co(NO_3)_2$ concentration of 10%, ultrasonic time of 2 h and calcination temperature of 550 °C remained unchanged is shown in Fig. 10. With increasing the calcination time, the breakthrough and saturated adsorption time both increased first and then decreased, reached the maximums at calcination time of 3 h, which are 7 min and 53 min, respectively. Similar to the effect of calcination temperature the overlong calcination time would lead to an aggregation of active Co_3O_4 and reduce exposed active sites, thus exhibit a poor H_2S removal efficiency. The saturated H_2S capacity and desulfurization rate of adsorbents exhibited the similar trends, which shows the maximum saturated H_2S capacity and desulfurization rate of 38.7 and 45.1%, respectively, at calcination time of 3 h.

3.2.3 Effect of adsorption conditions. The Co_3O_4/MCM-41-U was prepared using $Co(NO_3)_2$ concentration of 10%, ultrasonic time of 2 h, calcination temperature of 550 °C and calcination time of 3 h. The effect of adsorption time on performance of H_2S removal of Co_3O_4/MCM-41-U was evaluated at model gas flowrate of 20 mL min^{-1} in the fixed-bed reactor using 0.2 g of adsorbent (Fig. 11). With increasing the adsorption temperature, the breakthrough and saturated adsorption time both increased first and then decreased, reached the maximum at adsorption temperature of 45 °C (10 min). The breakthrough time at different adsorption temperatures was decreased in the order of 45 °C > 35 °C > 25 °C > 55 °C > 65 °C. This is because at excessive low adsorption temperature, the H_2S adsorbed onto adsorbent mainly *via* week van der Waals force by physical adsorption, which is usually reversible without selectivity. With increasing the adsorption temperature, the system temperature is able to provide enough energy to activate H_2S molecules, and the chemical adsorption *via* the strong

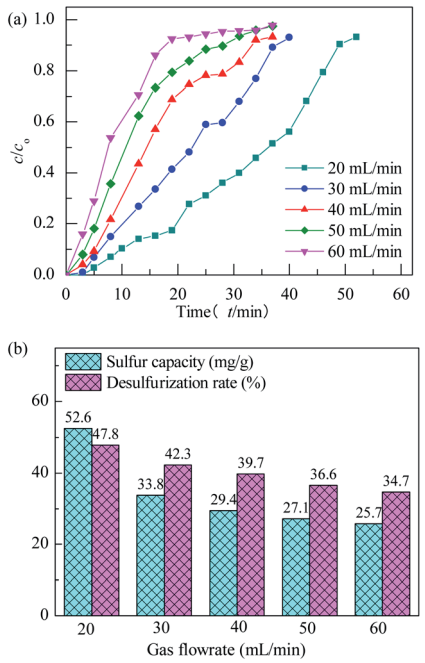

Fig. 12 H_2S breakthrough curves (a) and saturation sulfur capacity and desulfurization rate (b) of Co_3O_4/MCM-41-U at different gas flowrates.

This journal is © The Royal Society of Chemistry 2020

Open Access Article. Published on 17 August 2020. Downloaded on 2/10/2026 6:04:56 PM.
This article is licensed under a Creative Commons Attribution-NonCommercial 3.0 Unported Licence.

chemical bond gradually became the predominant adsorption mode. As a results, a much improved H_2S removal efficiency was observed. The saturated H_2S capacity and desulfurization rate of adsorbents exhibited the similar trends, which shows the maximum saturated H_2S capacity and desulfurization rate of 52.6 and 47.8%, respectively, at adsorption temperature of 45 °C.

The effect of model gas flowrate on performance of H_2S removal over Co_3O_4/MCM-41-U is evaluated at adsorption temperature of 45 °C in the fixed-bed reactor using 0.2 g of adsorbent (Fig. 12). With increasing the model gas flowrate, the breakthrough and saturated adsorption time both decreased, showing that increasing the gas flowrate would decrease the H_2S removal efficiency. This is understandable because the increase of gas flowrate, can eliminate the influence of external diffusion, but reduces the residence time of H_2S molecules in the fixed bed, which could cause some of the H_2S molecules are take away by the rapid flow before they are adsorbed onto adsorbent. In other words, the contact between H_2S molecules and adsorbent is inadequate, as a results, a decrease in the breakthrough and saturated adsorption time H_2S removal efficiency with increasing gas flowrate was observed. Therefore, appropriate gas flowrate is beneficial to H_2S purification. The saturated H_2S capacity and desulfurization rate of adsorbents exhibited the similar trends, which shows the maximum saturated H_2S capacity and desulfurization rate of 52.6 and 47.8%, respectively, at gas flowrate of 20 mL min^{-1}. The breakthrough time (τ_a) and saturated adsorption time (τ_e) were 10 min and 50 min at gas flowrate of 20 mL min^{-1}. It can be calculated by eqn (3) that for this situation, the mass transfer zone (MTZ) of Co_3O_4/MCM-41-U is about 240 mm.

3.2.4 Adsorption mechanism. Watanabe *et al.*[4] proposed that at ambient temperature H_2S removal from natural gas underwent through weak chemisorption over the activated carbon and zeolite/molecular sieve, while for metal oxides, such as ZnO, CuO, and Fe_2O_3, underwent through a dissociative chemisorption. Based on the reported adsorption mechanisms[44,45] and our previous study,[46] a possible mechanism of H_2S removal over Co_3O_4/MCM-41-U adsorbent can be described by the following steps (Scheme 4): (1) H_2S molecules are adsorbed over Co_3O_4/MCM-41-U surface. (2) Dissociation of H_2S into H^+ and HS^- or S^{2-} on Co_3O_4 active sites (eqn (5) and (6)); (3) subsequently sulfidation of the active Co_3O_4 by HS^- or S^{2-} leads to the formation of cobalt sulfide and water at the surface of adsorbent (eqn (7) and (8)).

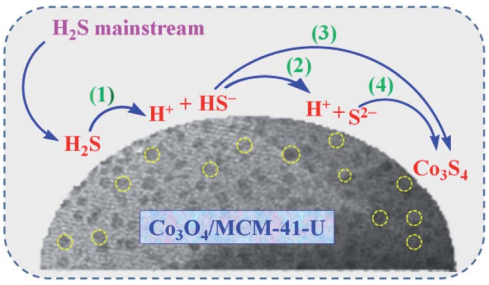

Scheme 4 Possible mechanism for the H_2S removal over Co_3O_4/MCM-41-U.

Table 2 Relation between regeneration times and desulfurization performance of Co_3O_4/MCM-41-U

Regeneration times	0	1	2
Breakthrough time (min)	10.0	9.6	9.1
Saturated H_2S capacity (mg g^{-1})	52.6	47.8	42.1
H_2S removal rate (%)	47.8	46.3	42.1

$$H_2S = H^+ + HS^- \quad (6)$$

$$HS^- = H^+ + S^{2-} \quad (7)$$

$$Co_3O_4 + 4HS^- + 4H^+ = Co_3S_4 + 4H_2O \quad (8)$$

$$Co_3O_4 + 4S^{2-} + 4H^+ = Co_3S_4 + 4H_2O \quad (9)$$

Formation of cobalt sulfide at the surface layers incorporating eqn (7) and (8)

$$Co_3O_4 + 4H_2S = Co_3S_4 + 4H_2O \quad (10)$$

3.2.5 Regeneration studies. Regeneration was performed *in situ*. Typically, the fixed-bed reactor with deactivated Co_3O_4/MCM-41-U was purged in a flowing nitrogen gas at 200 °C for 3 h and then cool down to the adsorption temperature. Relation between regeneration times and desulfurization performance of Co_3O_4/MCM-41-U is shown in Table 2. The breakthrough time of Co_3O_4/MCM-41-U after 2 times of regeneration decreased from 10.0 min to 9.1 min, which recovered by 91.0%. The recovered saturated H_2S capacity of Co_3O_4/MCM-41-U after 2 times of regeneration was 42.1 mg g^{-1}, still much higher than that of MCM-41, showing that the Co_3O_4/MCM-41-U possessed a good regenerability performance.

4 Conclusions

The Co_3O_4/MCM-41 adsorbents were successfully prepared by UAI and TMI technologies. XRD result demonstrated that UAI method promotes more and well defined highly dispersed active Co_3O_4 phase on MCM-41. All the adsorbents retained the mesoporous nature of MCM-41 with average pore diameter ranged in 2.75 to 374 nm after loading of Co_3O_4. The Co_3O_4/MCM-41-U which prepared *via* UAI method possessed much higher BET specific surface area and pore volume than those of Co_3O_4/MCM-41-T which prepared *via* TMI method. The fixed-bed adsorption desulfurization experiments showed H_2S removal was improved by loading Co_3O_4, showing that supporting active metal oxide on MCM-41 porous materials can take full advantages of metal oxides and MCM-41. The desulfurization performances decreased in the order of Co_3O_4/MCM-41-U > Co_3O_4/MCM-41-T > MCM-41. The Co_3O_4/MCM-41-U

Open Access Article. Published on 17 August 2020. Downloaded on 2/10/2026 6:04:56 PM. This article is licensed under a Creative Commons Attribution-NonCommercial 3.0 Unported Licence.

prepared using $Co(NO_3)_2$ concentration of 10%, ultrasonic time of 2 h, calcination temperature of 550 °C and calcination time of 3 h exhibited the best H_2S removal efficiency. At adsorption temperature of 25 °C with model gas flowrate of 20 mL min^{-1}, the breakthrough time of Co_3O_4/MCM-41-U was 10 min, and the saturated H_2S capacity and H_2S removal rate were 52.6 mg g^{-1} and 47.8%, respectively.

Conflicts of interest

The authors declared that they have no conflicts of interest to this work.

Acknowledgements

This work was supported by the National Natural Science Foundation of China (21276048).

References

1 A. S. Camara, S. F. Lütke, C. P. Pinheiro, M. L. G. Vieira, T. R. S. A. Cadaval Jr and L. A. A. Pinto, *Environ. Sci. Pollut. Res.*, 2020, DOI: 10.1007/s11356-020-09924-5.
2 M. L. G. Vieira, C. P. Pinheiro, K. A. Silva, S. F. Lutke, T. R. S. A. Cadaval, G. Dotto and L. A. A. Pinto, *Chem. Eng. Commun.*, 2019, **11**, 1474–1486.
3 G. Basina, D. A. Gaber, S. A. Yafei, V. Tzitzios, S. A. Gaber, I. Ismail, B. V. Vaithilingam, K. Polychronopoulou, S. A. Hashimi and Y. A. Wahedi, *Chem. Eng. J.*, 2020, **398**, 125585.
4 S. Watanabe, *Catal. Today*, 2020, DOI: 10.1016/j.cattod.2020.05.064.
5 S. Moioli, A. Giuffrida, M. C. Romano, L. A. Pellegrini and G. Lozza, *Appl. Energy*, 2016, **183**, 1452–1470.
6 S. J. Majeed, *J. Nat. Gas Sci. Eng.*, 2016, **36**, 175–183.
7 M. S. Shah, M. Tsapatsis and J. I. Siepmann, *Chem. Rev.*, 2017, **117**, 9755–9803.
8 A. Peluso, N. Gargiulo, P. Aprea, F. Pepe and D. Caputo, *Sep. Purif. Rev.*, 2018, **48**(1), 1–12.
9 S. Louhichi, A. Ghorbel, H. Chekir, N. Trabelsi and S. Khemakhem, *Appl. Clay Sci.*, 2016, **127**, 123–128.
10 J. Zhang, H. Song, Y. Chen, T. Hao, F. Li, D. Yuan, X. Wang, L. Zhao and J. Gao, *RSC Adv.*, 2018, **66**, 38124–38130.
11 M. M. Wu, L. Shi, W. Su, T. T. Lim, A. Vedsha, F. Yu, H. L. Fan and J. Mi, *Chem. Eng. J.*, 2018, **353**, 273–287.
12 A. Pourreza, S. Askari, A. Rashidi, A. Seif and M. Kooti, *Chem. Eng. J.*, 2019, **363**, 73–83.
13 M. M. Wu, T. Li, H. Y. Li, H. L. Fan and J. Mi, *Energy Fuels*, 2017, **31**, 13921–13932.
14 M. M. Wu, B. W. Chang, T. T. Lim, W. D. Oh, J. X. Lei and J. Mi, *J. Hazard. Mater.*, 2018, **360**, 391–401.
15 H. K. Jun, T. J. Lee, S. O. Ryu and J. C. Kim, *Ind. Eng. Chem. Res.*, 2001, **40**, 3547–3556.
16 Z. B. Huang, B. S. Liu, F. Wang and R. Amin, *Appl. Surf. Sci.*, 2015, **353**, 1–10.
17 A. S. Khder, H. Hma and M. S. Elshall, *Appl. Catal., A*, 2012, **411**, 77–86.
18 F. Farjadian, P. Ahmadpour, S. M. Samani and M. Hosseini, *Microporous Mesoporous Mater.*, 2015, **213**, 30–39.
19 T. Yasmin and K. Müller, *Microporous Mesoporous Mater.*, 2015, **208**, 83–92.
20 S. Bennici, A. Gervasini and V. Ragaini, *Ultrason. Sonochem.*, 2003, **10**, 61–64.
21 J. Dou, J. Yu, A. Tahmasebi, F. Yin, S. Gupta, X. Li, J. Lucas, C. Na and T. Wall, *Fuel Process. Technol.*, 2015, **135**, 187–194.
22 J. Mi, J. Ren and Y. Zhang, *Environ. Eng. Sci.*, 2012, **29**, 1026–1031.
23 M. R. AbuKhadra, A. S. Mohamed, A. M. El-Sherbeeny and M. A. Elmeligy, *J. Hazard. Mater.*, 2020, **389**, 122129.
24 K. Silas, W. A. W. A. K. Ghani, T. S. Y. Choong and U. Rashid, *Fuel Process. Technol.*, 2018, **180**, 155–165.
25 R. Apiratikul, *Process Saf. Environ. Prot.*, 2020, **137**, 58–65.
26 J. A. Cecilia, A. Infantes-Molina, E. Rodríguez-Castellón and A. Jiménez López, *Appl. Catal., B*, 2009, **92**(1), 100–113.
27 H. Song, J. Gong, H. Song and F. Li, *Appl. Catal., A*, 2015, **505**, 267–275.
28 P. V. Suraja, Z. Yaakob, N. N. Binitha, S. Triwahyono and P. P. Silija, *Clean Technol. Environ.*, 2013, **15**(6), 967–975.
29 X. Chen, Y. Chen, X. Luo, H. Guo, N. Wang, D. Su, C. Zhang, T. Liu, G. Wang and L. Cui, *Appl. Surf. Sci.*, 2020, **526**, 146626.
30 M. Thommes, K. Kaneko, A. V. Neimark, J. P. Olivier, F. Rodriguez-Reinoso, J. Rouquerol and K. S. W. Sing, *Pure Appl. Chem.*, 2015, **87**, 1051–1069.
31 X. Wang, X. Ma, L. Sun and C. Song, *Green Chem.*, 2007, **9**, 695–702.
32 X. Chen, X. L. Wang, G. Ran, Z. Cui, S. H. Chen and K. Xie, *Fine Chem.*, 2016, **33**(2), 188–194.
33 H. Zhao, J. Hu, J. Wang, L. Zhou and H. Liu, *Acta Phys.-Chim. Sin.*, 2007, **23**, 801–806.
34 A. Cecilia, *Appl. Catal., B*, 2009, **92**(92), 100–113.
35 Z. Liu, Y. Teng and K. Zhang, *J. Energy Chem.*, 2015, **24**, 322–330.
36 B. Pejova, A. Isahi, M. Najdoski and I. Grozdanov, *Mater. Res. Bull.*, 2001, **36**, 161–170.
37 Y. Li, X. Guo, G. Zhou, X. Lu, T. Cheng, T. Wu and K. Zhen, *Chin. J. Catal.*, 2005, **07**, 591–596.
38 C. Y. Chen, H. X. Li and M. E. Davis, *Microporous Mater.*, 1993, **2**(1), 17–26.
39 X. Wang, J. Jia, L. Zhao and T. Sun, *Water, Air, Soil Pollut.*, 2008, **193**(1–4), 247–257.
40 J. Goworek, A. Borowka, R. Zaleski and R. Kusak, *J. Therm. Anal. Calorim.*, 2005, **79**, 555–560.
41 H. Liu and S. K. Yen, *J. Power Sources*, 2007, **166**, 478–484.
42 F. Wyrwalski, J. F. Lamonier, M. J. Pere-zurita, S. Siffert and A. Aboukaïs, *Catal. Lett.*, 2006, **108**(1–2), 87–95.
43 A. Gedanken, *Ultrason. Sonochem.*, 2004, **11**, 47–55.
44 J. Zhang, G. Wang, W. Wang, H. Song and F. Li, *Res. Chem. Intermed.*, 2016, **42**, 6003–6012.
45 E. Laperdrix, G. Costentin, O. Saur, J. C. Lavalley, C. Nédez, S. Savin-Poncet and J. Nougayrède, *J. Catal.*, 2000, **189**, 63–69.
46 H. Fang, J. Zhao, Y. Fang, J. Huang and Y. Wang, *Fuel*, 2013, **108**, 143–148.

 This journal is © The Royal Society of Chemistry 2020